

## Thermal convection with a freely moving top boundary

Jin-Qiang Zhong

*Department of Physics, New York University, 4 Washington Place, New York, New York 10003*

Jun Zhang<sup>a)</sup>

*Department of Physics, New York University, 4 Washington Place, New York, New York 10003  
and Applied Mathematics Laboratory, Courant Institute, New York University, 251 Mercer Street,  
New York, New York 10012*

(Received 8 May 2005; accepted 29 September 2005; published online 22 November 2005)

In thermal convection, coherent flow structures emerge at high Rayleigh numbers as a result of intrinsic hydrodynamic instability and self-organization. They range from small-scale thermal plumes that are produced near both the top and the bottom boundaries to large-scale circulations across the entire convective volume. These flow structures exert viscous forces upon any boundary. Such forces will affect a boundary which is free to deform or change position. In our experiment, we study the dynamics of a free boundary that floats on the upper surface of a convective fluid. This seemingly passive boundary is subjected solely to viscous stress underneath. However, the boundary thermally insulates the fluid, modifying the bulk flow. As a consequence, the interaction between the free boundary and the convective flow results in a regular oscillation. We report here some aspects of the fluid dynamics and discuss possible links between our experiment and continental drift.

© 2005 American Institute of Physics. [DOI: 10.1063/1.2131924]

### I. INTRODUCTION

When an upward heat flux passes through a fluid, the thermal energy is transported in two ways: conduction and convection. In conduction, the fluid stays put, as if it were a solid. In a gravitational field, if the heat flux exceeds a threshold, instability due to buoyancy causes convection.<sup>1</sup> The instabilities originate mostly near the top and the bottom boundaries, which cool and heat the bulk fluid. In these regions, hot fluid becomes lighter and tends to rise; cold fluid becomes denser and tends to descend. Due to mass transport, convection transports heat more efficiently than conduction. The control parameter that selects between the two regimes is the Rayleigh number  $Ra$ , a dimensionless ratio of the buoyant driving and dissipative mechanisms,<sup>2</sup> including viscous and thermal dissipation:

$$Ra = \frac{\alpha g \Delta T D^3}{\nu \kappa},$$

where  $g$  is the gravitational acceleration,  $\Delta T$  is the temperature difference between the bottom and the top,  $D$  is the depth of the fluid, and  $\alpha$ ,  $\nu$ , and  $\kappa$  are the thermal expansion coefficient, the kinematic viscosity, and the thermal diffusivity of the fluid, respectively. For large  $Ra$ , the convective flow becomes turbulent.<sup>3</sup> At  $Ra \sim 10^7$ , a large-scale circulation emerges,<sup>4,5</sup> and this large-scale turbulent eddy in the bulk entrains thermal plumes. At the same time, thermal plumes feed the circulation and sustain the mean flow.

Thermal convection is ubiquitous in nature, from a heated room or the air above a burning candle to the internal dynamics of stars and planets. Earth and Mars<sup>6,7</sup> are geologi-

cally active. The temperature difference between the hot interior and the cooler surface drives their mantle layers. As a result, mantle convection ultimately drives all geological events, such as volcanoes, earthquakes, and plate tectonics.<sup>8</sup>

To understand in detail plate-tectonic mechanisms and the interactions between the continents and the convective mantle is challenging. Material transport couples with heat exchange and dynamic boundary conditions, making analytical descriptions infeasible. Numerical simulations have played a major role in clarifying these complicated dynamics, capturing features like continental collision, breakup, aggregation, and dispersion.<sup>9-11</sup> According to some numerical simulations, continental motion results from two coupled mechanisms.<sup>9,10,12</sup> First, mantle convection drives continents to new positions. The continents, in turn, modify the flow inside the mantle due to "thermal blanketing."<sup>13-15</sup> Can a laboratory experiment produce similar behaviors and rich dynamics?

Previous experimental simulations of the dynamics of the Earth addressed geological events such as plate collisions, continental faulting,<sup>16</sup> lithosphere subduction,<sup>17</sup> sea floor spreading,<sup>18,19</sup> and the sustained motion of a floating model continent with a heat source attached underneath.<sup>20</sup> These fluid experiments generally have moving but externally driven boundaries. In our current study, the intrinsic forces of the convective flow cause boundary motion. Apart from gravity, no external force causes boundary motion.

In a previous experiment, we studied the interplay between a free boundary and a convective fluid. For high Rayleigh numbers, the floating boundary oscillated,<sup>21</sup> as in a geophysical phenomenon conjectured by Wilson in 1966. Wilson's model<sup>22</sup> proposed that large continents migrated over the past 2.5 billion years in a nearly periodic fashion.

As in our previous experiment,<sup>21</sup> a freely moving top

<sup>a)</sup> Author to whom correspondence should be addressed. Telephone: 212 998 7776. Fax: 212 995 3639. Electronic mail: zhang@physics.nyu.edu

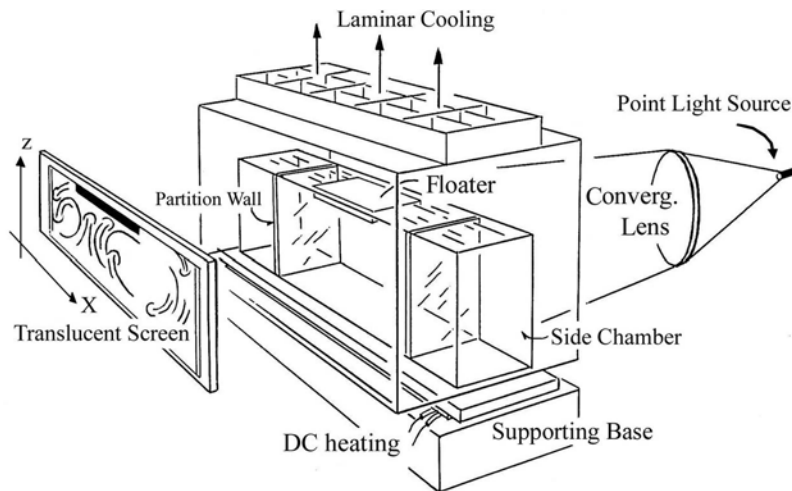


FIG. 1. Experimental setup. An elongated water tank is heated uniformly from the bottom and cooled at the free surface with a laminar-flow cooling hood. Two vertical partitions separate the tank into three chambers. A free-moving boundary (floater) floats above the middle section of the convection cell. The convective flow is visualized by shadowgraph and the position of the floating boundary recorded.

boundary interacts with a convective fluid. Here, we discuss a broader range of phenomena more thoroughly and quantitatively, including oscillation periodicity, flow fields, temperature distributions, and the relation to terrestrial plate tectonics.

## II. EXPERIMENTAL DESIGN AND METHODS

Figure 1 shows our experiment. A heater heats a glass water tank, which is 60 cm long, 7.8 cm wide, and 12.2 cm high, from below uniformly. The dc power supply provides constant-power heating. At the top, a floating boundary covers part of the open fluid surface. A custom-built laminar air hood cools the top of the convection cell. A row of cooling fans at the top of the hood removes heat from the free surface of the convective fluid.

To prevent heat loss at both ends of the convection cell and to ensure ideal thermal boundary conditions, we partition the 60 cm long tank into three chambers. The middle chamber—our working convection cell—has inner dimensions of 36.5 (length  $L$ ), 7.8 (width), and 11.3 (fluid depth,  $D$ ) cm. Water permeates slowly between the chambers through thin gaps between the partitions and the glass walls. Since the fluid in each chamber experiences the same heating from below and cooling from above, lateral heat exchange between sections is negligible. The side partition walls are fully submerged; a 0.7 cm deep fluid layer connects the three chambers. To compensate for unavoidable water evaporation, a service tank outside the laminar hood maintains a fixed water level, supplying water to the convection cell through a siphon (see the Appendix, Sec. 1), to maintain an aspect ratio of  $L/D=3.2$ . For simplicity, we keep this aspect ratio fixed throughout this experimental study.

The floating boundary (floater) is acrylic plastic (Lucite). Despite being denser ( $\rho=1.18 \text{ g/cm}^3$ ) than the fluid, it floats due to surface tension. The floating boundary has sharp edges on all sides, which, since clean acrylic is slightly hydrophobic, stop the invasion of the fluid contact lines. For the shape and properties of the floater see the Appendix, Sec. 2. Here, we regard the floating boundary as a rigid, rectangular block, 6.9 cm wide along the short side of the convec-

tion cell. Its length ( $l$ ) can be changed from 3.6 to 21.4 cm in steps, corresponding to a coverage ratio ( $CR=l/L$ ) of 0.1 to 0.6 over the free fluid surface.

Clean water wets the vertical glass walls of the convection cell; the meniscus curves up, while the meniscus on the relatively heavy floater curves down. The interactions of the menisci repulse the floater from the glass walls,<sup>23</sup> centering the floater along the short side (width) of the convection cell, leaving a 4.5 mm fluid gap on each side. The partition walls, though submerged under water, constrain the floater. Along the long side of the convection cell the floater experiences a flat potential until it hits the partition walls. As a result, the floater moves only in one dimension, affected only by the viscous fluid force at its base.

The convective flow and the position of the floating boundary are visualized and recorded with a shadowgraph technique<sup>24</sup> and a time-lapse, black-and-white video camera. A custom-written computer program then tracks the position of the floating boundary, its velocity, and the flow velocity.

We use semiconductor thermistors (GE-AB6E3-BR11KA502R) to measure local temperature distributions. The diameter of the thermistors is about  $d=0.5 \text{ mm}$ . Their response time is on the order of 15 ms ( $d^2/4K_{th}$ , where  $K_{th}$  is the heat diffusivity of the solid thermistors), limiting the sampling frequency to 70 Hz. A Wheatstone bridge and a lock-in amplifier measure fluid temperature to better than 0.1 K. Besides thermistors, we use thermochromic liquid crystal beads that qualitatively show temperature distributions by the color and intensity of the light they scatter.<sup>25,26</sup>

We use a number of methods to measure flow speed. A laser Doppler velocimeter (TSI-LDP100) measures the time series of velocity at a single point. Recorded video frames and tracking of thermal structures such as individual plumes also give flow speeds. Long exposures of flow tracers yield track patterns that portray the flow field.

Often we measure fluid velocity and temperature in parallel. Correlating instantaneous measurements clarifies the dynamics.

We rigorously tested our apparatus to check that neither the cooling mechanism nor the surface tension effect moved

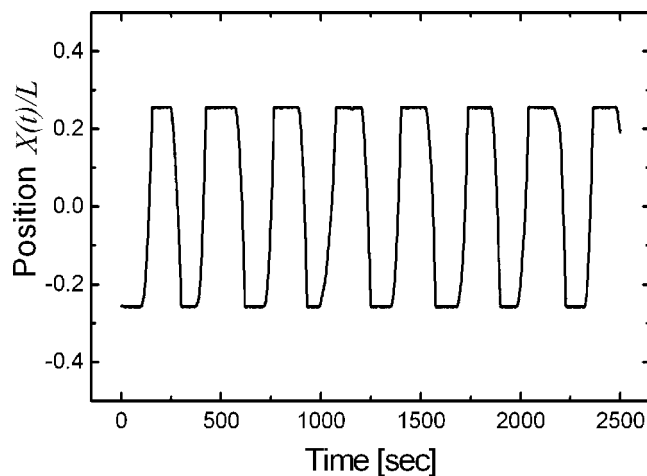


FIG. 2. Floating boundary position, normalized by the convection-cell length, vs time. The floating boundary covers 50% of the free surface and  $Ra=1.1 \times 10^9$ . Oscillation is nearly periodic even though the thermal convection is turbulent. Each period has two distinct time scales: a transient time during which the free boundary moves from one side to the other and an organization time when the floating boundary stays put.

the floating boundary. This ensures that any floater motion would be directly a result of viscous drag from underneath.

### III. OBSERVATIONS FROM EXPERIMENTS

Figure 2 shows the position of the floating boundary, which covers half the length of the free fluid surface. The floater and the convective fluid oscillate nearly periodically, for  $Ra=1.1 \times 10^9$ , and Prandtl number,  $Pr=\nu/\kappa$ , equals 3. The average period for the oscillation is 320 s. The oscillation is extremely robust, lasting for days and hundreds of periods. After external perturbation, the oscillation resumes within minutes. A regular oscillatory state has emerged from a highly turbulent convective fluid.

To better understand this intriguing boundary oscillation, we first focus on a convection cell with no solid boundary on the top surface, a Bénard-Marangoni convection,<sup>27,28</sup> then on a cell with a fixed top boundary, unable to respond to fluid forces. We finally discuss the oscillatory state and explain its mechanism.

#### A. Convection with a free fluid surface, without a free, solid boundary

Without a floating boundary, at high Rayleigh number ( $1.1 \times 10^9$ ) and aspect ratio 3.2, the convective pattern assumes one of four stable states. In one, along the long side of the convection cell, a large-scale flow rises from one side and descends on the other so a single turbulent eddy occupies the entire convection cell (with aspect ratio  $\sim 3$ ). Left-right symmetry produces two such states. This single-eddy pattern survives for at least 24 h. The other two states have two eddies; the flow ascends/descends in the middle of the cell and descends/ascends close to the partition walls. These two patterns can also survive for days. To create such patterns, we partially cover the convection cell with Styrofoam sheets or even mechanically disturb it. We then remove all external influences before observation of flow patterns. It

appears that all four states observed above are stable; what survives in the system depends only on the initial condition (the history).

We also test plausible three-eddy patterns, for example, a counterclockwise eddy on the left, a clockwise eddy in the middle, and a counterclockwise eddy on the right. These patterns are not stable, converting to one of the four patterns above within 80 min. These stable patterns resemble convective patterns at low Rayleigh numbers.<sup>28</sup>

A very small passive floating object placed on a free fluid surface will be carried by the flow and move to a position where the fluid descends into the bulk. Indeed, a small floating boundary with  $l/L=0.1$  maintains its position and does not affect the flow pattern for many hours. However, as we will demonstrate in the following sections, when the floater size is large enough, a freely moving floating boundary destabilizes all four stable flow patterns, even for boundaries small compared to the total fluid surface area or depth. For example, when  $l/L \sim 0.2$  or  $l/D \sim 0.6$ , the floating boundary modifies and destabilizes the large-scale convective flow.

#### B. Convection with a fixed, partially covering boundary at the top

We now examine the thermal perturbation a partial boundary at the top surface introduces. We first fix the floating boundary at one extremity of the convection cell. Regardless of the initial flow pattern, the bulk fluid soon develops an upwelling under the floating boundary and a descending flow under the open surface. At long times, in dynamic equilibrium a single eddy occupies the entire convection cell (aspect ratio  $\sim 3$ ). The time for a fluid particle to travel completely around a large-scale eddy defines the circulation period. The equilibration time is a few tens of circulation periods. During this time, the top and bottom boundaries communicate through the bulk fluid.

At  $Ra=1.1 \times 10^9$ , the temperature difference between the heated bottom and the free fluid surface is  $\Delta T=8.0$  K. Figure 3 shows two vertical temperature profiles (see Fig. 13 in the Appendix for measurement positions): under the partial floating boundary and under the free fluid surface. The fluid temperature under the floating boundary is higher than that in the rest of the fluid by 0.7 K or 9% of  $\Delta T$ . At the heated bottom, the horizontal temperature difference is less than 0.2 K, about 2% of  $\Delta T$ . The warmer fluid below the insulating boundary rises and the relatively cold fluid below the free fluid surface descends. A large-scale flow pattern emerges. Figure 4 shows a vertical scan of the horizontal velocity component, under the floating boundary, fixed at the left side of the convection cell. At this position, the flow essentially moves upward so the horizontal speed is less than the average speed of the eddy (about 1.8 cm/s). The large-scale circulation in the bulk shows up as a rightward flow under the floating boundary and a leftward flow near the bottom plate. We notice that this velocity profile is not symmetric about the midheight of the fluid.

The temperature and velocity asymmetries are due to the asymmetric cooling rates along the upper side of the convec-

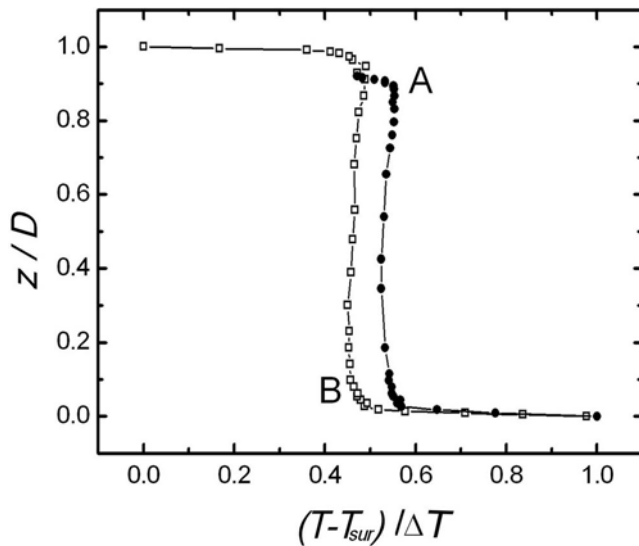


FIG. 3. Two vertical temperature profiles in the convection cell, for  $Ra = 1.1 \times 10^9$ . Solid circles (A): profile under the centre of a fixed floating boundary that covers 50% of the surface area of the convection cell on the left side. Open squares (B): profile under the open fluid surface. At each position, the value represents an average of a 120 s measurement at 10 Hz sampling rate.  $\Delta T$  is the temperature difference across the convection cell,  $T_{sur}$  is the average temperature on the free fluid surface, and  $D$  is the fluid depth. Measurements carried out after more than 3 h of relaxation. See the Appendix (Fig. 13) for measurement positions.

tion cell. At the open fluid surface, fluid mixing enhances heat loss, speeding cooling. The cooled fluid is heavier and descends. Fluid under the solid boundary is protected from losing heat, and a viscous boundary layer inhibits mixing of fluid due to the no-slip boundary condition. So heat is transported through both the solid boundary and the viscous boundary layer by conduction, which is much less efficient. Descending cold fluid under the open fluid surface and as-

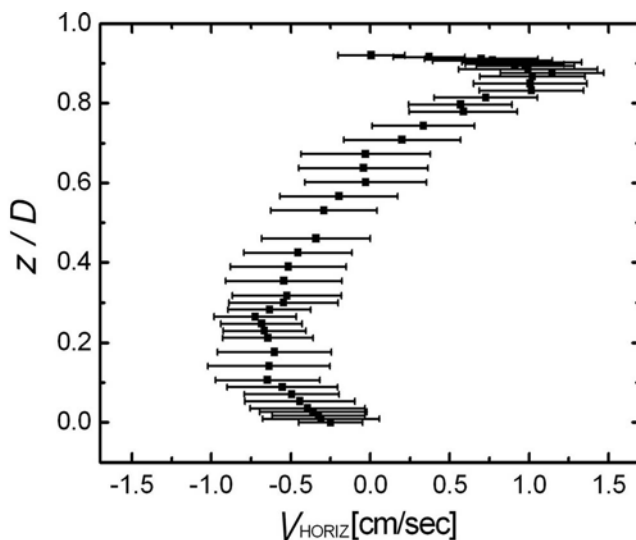


FIG. 4. The average vertical profile of the horizontal velocity component across the convection cell, at  $Ra = 1.1 \times 10^9$ . Velocities are measured under the fixed floating boundary that covers 50% of the upper surface. The boundary is fixed at the left side of the convection cell. Error bars show rms velocity fluctuations.

ending warmer fluid under the floating boundary slowly form a large-scale circulation. Both the warm and cold flows feed the large-scale circulation and sustain it. In return, the large-scale circulation entrains both reinforcing flows by pushing both into certain locations. Eventually the limited thermal driving balances dissipation factors, such as viscous friction.

The solid floating boundary reduces local heat transport. In geophysics, this phenomenon is called the “thermal blanketing effect.”<sup>14,29,30</sup> Large continents are more rigid than the convective mantle and oceanic plates. Continents are lighter and also thicker than the oceanic lithosphere so they effectively trap heat by prohibiting convective currents from reaching the surface of the Earth. The thermal blanketing effect forms hot spots around the globe, especially under large continents<sup>29</sup> (presently most hot spots are observed under the ocean since large continents have drifted away). Numerical simulations show that the effects of thermal blanketing can reverse mantle convection patterns at scales larger than the continents.<sup>9,10</sup>

### C. The consequences of the thermal blanketing effect

The vertical temperature profile (Fig. 3) yields the thickness of the thermal boundary layer within which the temperature varies in a linear fashion. From the thermal boundary thickness and temperature drop, we calculate the heat flux through the bottom of the convection cell and under the floating boundary. At  $Ra = 1.1 \times 10^9$ , the heat flux is  $250 \text{ W/m}^2$  under the floating boundary, which is 9% of the flux through the bottom boundary layer. Most of the heat is lost through the free fluid surface, at a rate of about  $2100 \text{ W/m}^2$ . The heat loss contrast between the covered surface and the exposed surface is about 1:8. For smaller Rayleigh numbers (say,  $Ra = 2 \times 10^7$ ), this contrast is only 1:3. The heat transport contrast in our experiment is of the same order of magnitude as that in terrestrial geology where the contrast of the heat flux through the continental lithosphere to that through the oceanic lithosphere is estimated<sup>14,30</sup> to be 1:10.

Within the viscous boundary layer, the viscous force exerted on the floating boundary is  $F \sim AU\eta/\lambda_v$ , where  $A$  is the area exposed to the underlying flow,  $U$  is the flow speed just outside of the viscous boundary layer,  $\eta$  is the dynamic viscosity, and  $\lambda_v$  is the thickness of the viscous boundary layer. For our floating boundary size, flow-speed profile, and fluid viscosity, the typical force is on the order of a few dynes.

The strength of thermal activity varies with height. At the interface between the thermal boundary layer and the bulk, where thermal plumes detach from the heated plate (bottom) and cooled surface (top), temperature fluctuation is significant. The root-mean-squared (rms) (the second moment of the time series) temperature signal measures local thermal activity. Figure 5 shows vertical profiles of the rms temperature fluctuation at two locations, one under the floater and the other under the free fluid surface. For each point in the figure, we record a 2-min-long temperature time series at a 10 Hz sample frequency.

The profile of rms temperature fluctuation under the free

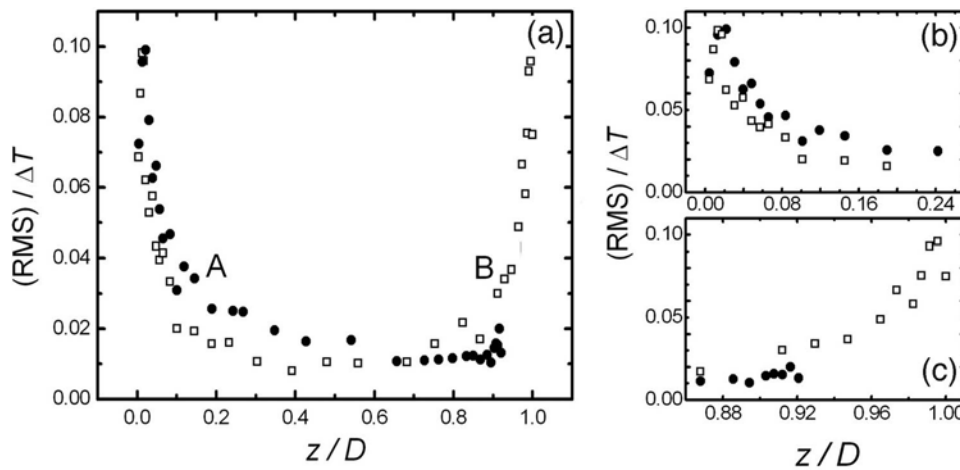


FIG. 5. (a) The vertical profile of rms temperature fluctuations in the convection cell, using the same data as in Fig. 3. Open squares (B): data under the open fluid surface, showing symmetric fluctuation at the bottom and near the surface. Solid circles (A): the profile under the fixed floating boundary; its rms is at its minimum near the floating boundary, indicating few thermal events. (b) Close up near the heated bottom, showing a thermal boundary layer thickness of about 2 mm. (c) Near the free surface, the rms fluctuation peaks around 0.5 mm below the air-fluid interface.

fluid surface (open squares) indicates that thermal activity increases near both the top and bottom thermal boundaries. Both layers show a similar level of activity. This profile of rms temperature fluctuation also reveals symmetry, even though the top-bottom symmetry is broken. The vertical profile under the thermally insulating boundary is asymmetric (solid circles). Though the rms amplitude at the bottom equals that under the free fluid surface, it is much reduced under the floater because of the low heat leakage upward (“thermal blanketing”).

The same time series measurements of local temperatures across the cell also give the “sign” or “direction” of the thermal transport. The *skewness* of temperature at each point (the third moment of the time series) is positive when the time series contains more positive “spikes” and vice versa. Figure 6 shows two temperature skewness profiles, derived from the same time series as Figs. 3 and 5. Under the free

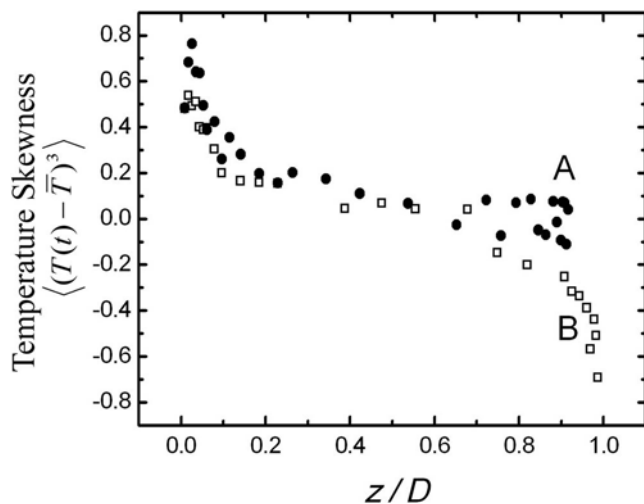


FIG. 6. The temperature skewness (the third moment) in the convection cell, using the same data as in Figs. 3 and 5. The open squares (B) show the distribution under the free fluid surface. The antisymmetry indicates that the emission frequency of hot plumes from the bottom is nearly the same as for the cold plumes from the free fluid surface. The heated bottom below the covered boundary (solid circles, A) has significantly greater hot plume emission than other positions. The skewness decreases to a low level near the center of the convection cell and remains roughly the same under the floating boundary.

surface, the profile is essentially antisymmetric. Near the bottom, the random passage of hot thermal plumes skews the temperature measurement positive. Near the top, cold plumes descending from the free surface skew the temperature negative. In the middle, the bulk fluid experiences the passage of equal numbers of hot and cold plumes, so the temperature skewness approaches zero.

Like the rms fluctuation, the skewness of the temperature also diminishes under the insulating “thermal blanket.” Thermal activity is consistently small due to the small heat loss through the cover.

An insulating cover (floating boundary) induces an asymmetric temperature distribution and distorted flow pattern due to “thermal blanketing.” These changes, as we show below, exert forces modifying the position of the floating boundary. The once stable convective flow self-excites a robust oscillation due to the freedom of movement of the floating boundary.

#### D. Thermal convection with a freely moving top boundary

With a free boundary, we observe the quasiregular oscillations of Fig. 2. At first glance, regularity of an oscillation driven by turbulence is somewhat puzzling. However, Secs. III B and III C showed that a thermal insulating boundary induces a large-scale flow, which dominates the stochastic turbulence. We now explain the essential physical mechanisms behind this nearly periodic state.

##### 1. The regular oscillation associated with the fluctuating temperature and velocity

We visualize the convective flow (Fig. 7) using cholesteric liquid-crystal beads evenly suspended in the fluid bulk, taking four snapshots at times indicated in Fig. 8. Figure 7(a) shows an instant when the floater starts to move to the left. A hot, upwelling flow is clearly visible below the floating boundary. A dominant counterclockwise (CCW) eddy occupies roughly 75% of the fluid bulk, compressing and weakening the clockwise (CW) eddy on the right. After the floater arrives at the left end of the chamber, the CCW eddy on the left quickly shrinks as the CW eddy on the right expands.

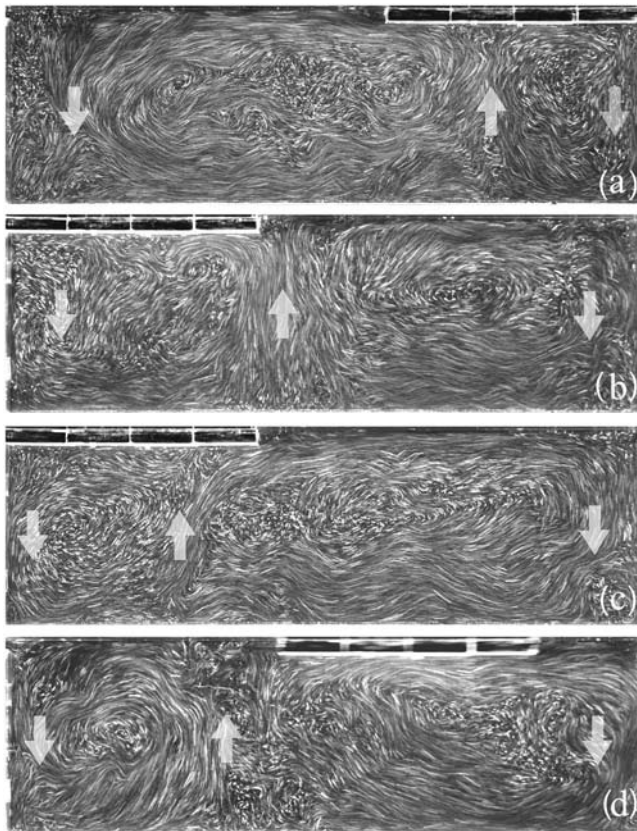


FIG. 7. Visualization of convective flow inside the fluid cell together with the floating boundary. Here,  $Ra=1.1 \times 10^9$ , and the boundary covers 40% of the upper fluid surface ( $CR=0.4$ ). Each photo uses a long exposure of 1.3 s. We see illuminated liquid-crystal  $30 \mu\text{m}$  beads. (a) Just before the free boundary is entrained toward the left; (b) after the floating boundary arrives at the left side of the cell; (c) shortly before the boundary starts to move to the right; (d) while moving to the right. See Fig. 8(a) for corresponding moments during an oscillation period.

Between the two eddies, the upwelling flow moves steadily to the left [Fig. 7(b)] until it reaches the center of the floating boundary. This flow-pattern reorganization takes 4–50 rounds of flow circulation, depending on the Rayleigh number and, more sensitively, on the floating-boundary size. If the size is about  $0.6L$ , the system needs a few circulations to adapt a new flow pattern. If the size is  $0.2L$ , however, it takes up to 30–50 circulations. During the reorganization, the net force applied to the floater points towards the left partition wall. In Fig. 7(c), symmetrically, the CW eddy on the right begins to dominate the bulk fluid, applying a rightward viscous drag on the floating boundary. As a consequence, the floating boundary starts to move back to the right [Fig. 7(d)], when the net force applied onto it changes sign. This process continues, and the oscillation persists.

During this oscillation, the velocity measured at the mid-bottom position inside the cell changes direction at the same frequency. Figure 8 shows instantaneous measurements of both the floater position and the horizontal velocity component. We see that the velocity signal at the bottom does not immediately reflect the departure of the floating boundary. But as soon as the boundary arrives at one side (say, the right side), the flow velocity at the bottom starts to change slowly from CW to CCW. The velocity time series in Fig. 8 is left-

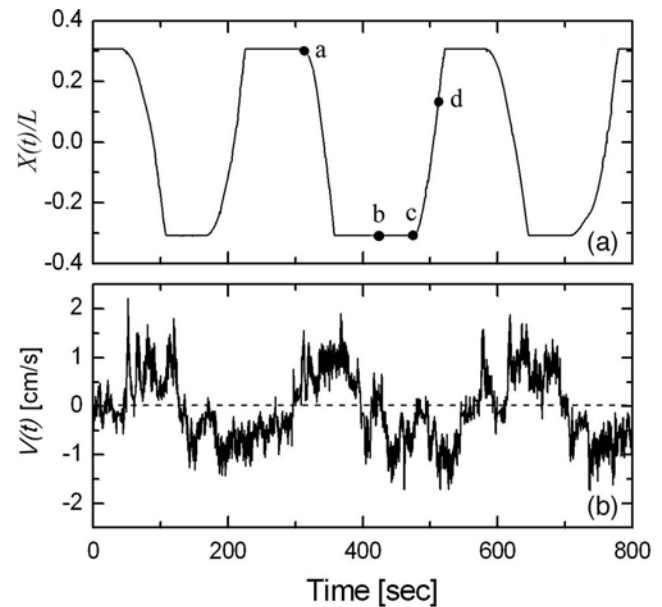


FIG. 8. At  $Ra=1.1 \times 10^9$  and  $CR=0.4$ , (A) position of the free boundary and (B) the corresponding velocity time series measured at the mid-bottom position of the convection cell (0.5 cm above the bottom and in the middle of the cell). The local velocity direction changes twice within one oscillation period. Letters (a, b, c and d) shown in (A) indicate when the photos in Fig. 7 were taken. Rightward movement corresponds to positive velocity.

right symmetric, due to the left-right symmetry of the measuring position and the regular oscillation. Unlike the case of a fixed floating boundary (Sec. III B), in the oscillatory state we always observe two coexisting turbulent eddies. During the oscillation, one eddy extends at the expense of the other. Before the small eddy is eliminated entirely, the viscous forces exerted by the evolving flow pattern move the floater away and the process reverses.

Figures 9(a) and 9(b) show instantaneous measurements of the floater position and the temperature near the upper-right corner of the convection cell (4.3 cm below the fluid surface, 7 cm left of the right partition wall). When the floater starts to leave the upper-left corner, cooling of the exposed fluid at the upper-right corner starts to weaken because of the approaching insulating boundary, which reduces the area of free fluid surface; the temperature at the upper-right corner then starts to rise from its lowest point. While the floating boundary stays put, the temperature climbs steadily due to minimal heat loss upward, reaching a maximum as the floater starts to leave, when the strength of the upwelling flow and the size of its corresponding CCW eddy are maximal. As soon as the floater departs from above the measuring position, the temperature declines as a result of cooling at the fluid surface. During the remaining half of the period, the temperature decays to its minimum.

The oscillation stands out above a background of turbulent thermal fluctuations. In Fig. 9(c) we calculate the dimensionless skewness of the temperature:

$$S(t) = \frac{\langle [T(t) - \bar{T}]^3 \rangle}{\langle [T(t) - \bar{T}]^2 \rangle^{3/2}}.$$

$S$  is positive while the floating boundary stays above the measuring point, as hot plumes accumulate, and becomes

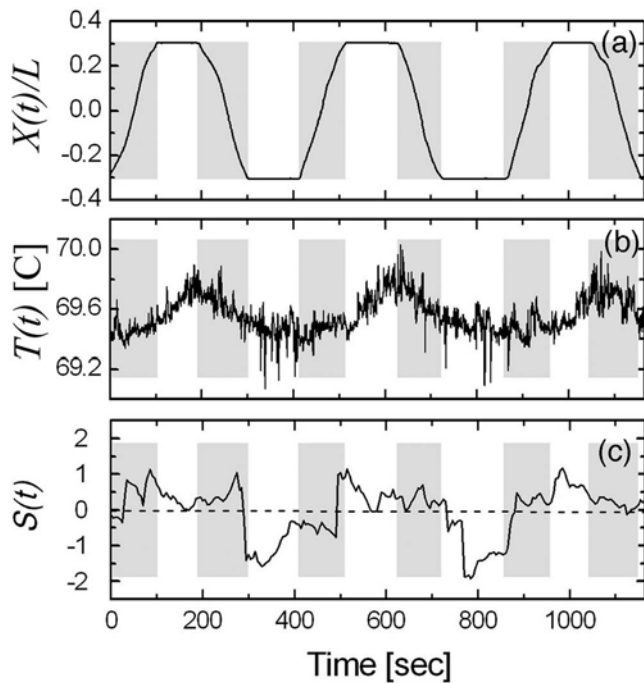


FIG. 9. (a) Instantaneous position of the free boundary. (b) Time series of temperature measurements at a fixed location (7 cm from the right partition and 4.3 cm below the free fluid surface). (c) The skewness calculated from the time series. Both the temperature signal and its skewness oscillate synchronously with the position of the free boundary. Here,  $Ra=1.6 \times 10^9$ ,  $CR=0.4$ . To guide the eye, the gray shade highlights the transit times.

negative as the boundary moves away, when cold plumes start to form and pass by. This change of sign of the skewness clearly indicates both global flow change and local flow reversal. Here, the pointwise measurement of a scalar temperature can reveal the flow direction of the thermal convection because hot fluid rises while cold descends.<sup>31,32</sup>

## 2. The oscillation frequency depends on the flow speed and Rayleigh number

Recent experiments and theories have shown a power-law relation between the average speed and the Rayleigh number.<sup>33–35</sup> Changing the flow speed directly affects the period of oscillation. In our experiment, each period consists of two time scales (Figs. 2, 8, and 9): the flow reorganization time and the boundary transit time. During the flow reorganization time (waiting period), the free-moving boundary stays at one side of the convection cell, touching the partition wall. During the transient time, the boundary moves from one end to the other. For higher flow speeds, the flow reorganization time should be shorter, assuming flow reorganization takes a relatively fixed number of circulations around the convection cell. Also, given the fixed boundary size and transit distance between the two ends, the transit time should be inversely proportional to the convective flow speed.

For a fixed boundary size, Fig. 10(a) shows the measured average oscillation period as a function of the Rayleigh number over almost two decades. Figure 10(b) shows separately the average reorganization time and the transit time.

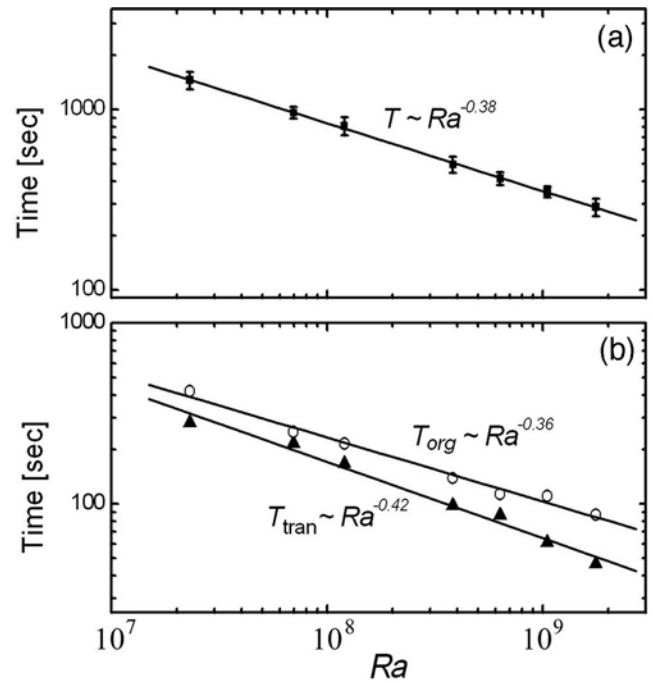


FIG. 10. (a) Scaling of the oscillation period as a function of the Rayleigh number. The floating boundary size is fixed at  $CR=0.5$ . (b) The transit time ( $T_{\text{tran}}$ , solid triangles) and the organization time ( $T_{\text{org}}$ , open circles), are also shown separately as a function of the Rayleigh number. Over about two decades, the data suggest power-law dependencies on  $Ra$ , with powers of about  $-0.42$  and  $-0.36$ , respectively.

The transit time scales with the Rayleigh number as  $T_{\text{tran}} \sim Ra^{-0.42}$ , in good agreement with previous works<sup>33–35</sup> that found  $Re \sim Ra^{0.40-0.47}$ .

## 3. The floating boundary size affects the oscillation frequency

The size of the floating boundary determines the amplitude of the thermal perturbation to the bulk. For a sufficiently small floating boundary, the thermal perturbation—the thermal blanketing effect—is too small to affect the bulk convection. The free boundary passively traces the flow (Sec. III A). As the boundary size increases, the thermal feedback becomes more effective. Meanwhile, the changes of the flow pattern and, consequently, the boundary oscillations become more deterministic. Figure 11 (left) illustrates these changes as we increase the floating boundary size from  $0.2L$  to  $0.5L$ . The boundary motion reversal or oscillation seems to be quite stochastic when the boundary size is small. As we increase the boundary size, the oscillation period becomes shorter and more regular.

As we change the floating boundary size at fixed Rayleigh number, even though the flow speed remains approximately constant, the speed of the boundary during transitions changes. Figure 11 (right) shows a velocity time series, normalized by the average flow speed. When the coverage ratio is 0.2, the floater speed occasionally approaches 55% of the flow speed. As the size of the floater increases, however, the floater speed decreases monotonically. At a coverage ratio of 0.5, the maximum speed drops to about 25% of the flow speed.

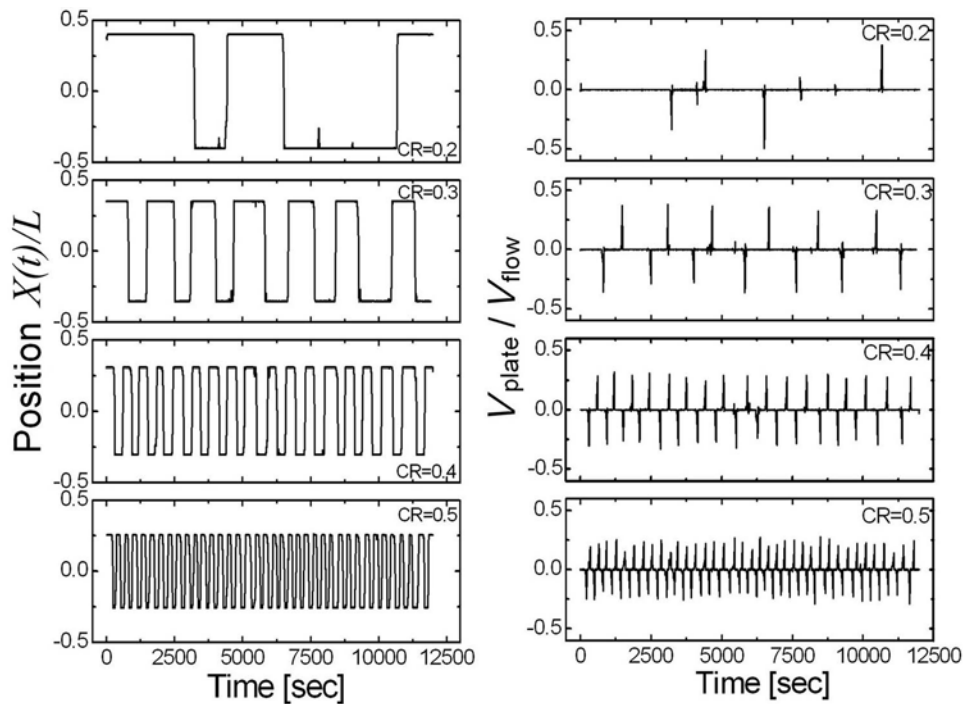


FIG. 11. (Left) At  $Ra=1.1 \times 10^9$ , the oscillation period decreases with increasing floating boundary size, while the oscillation becomes more regular. (Right) The corresponding instantaneous floater speed, normalized by the flow speed, decreases as the floating boundary size increases.

A naïve argument suggests that a large floating boundary experiences a proportionally larger force, giving a similar acceleration due to its larger mass. However, the free distance for the boundary to gain speed is greater for a small boundary. Also, a small boundary often experiences a pure unidirectional flow with better entrainment. The relatively large surface of a large boundary experiences flows in both directions. The force due to shear stress on the bottom of the boundary is

$$F_x = \int_S \sigma_{xz} dA = \eta \int_S \frac{\partial V_x}{\partial z} dA.$$

The index  $x$  points to the right, along the long axis of the convection cell. Here,  $\sigma_{xz}$  is the viscous stress tensor, which reduces to  $\eta(\partial V_x / \partial z)$  near a rigid boundary. The integral covers the entire bottom area of the floating boundary. The direction of the viscous drag from the turbulent flow varies, so we expect the transient speed to behave as shown in Fig. 11 (right).

Figure 12 shows the spread of the oscillation periods, normalized by the average period  $\langle T \rangle$ . The half-height width of each distribution decreases from 0.5 to about 0.25 as the floater size increases, so the oscillatory “clock” that emerges from the turbulent flow becomes more regular. When the floating boundary size is small, the flow reorganization and boundary transit are more susceptible to local flows like individual plumes, so the oscillations reveal the stochasticity of the turbulent flow. For a large floating boundary, a single plume contributes relatively little to the total viscous drag, which has the effect of averaging the fluctuations and causing more regular oscillations. This observation is to some extent analogous to the law of large numbers: the spread of the mean of a greater number of like distributions is smaller.<sup>36</sup>

Figure 12 also shows that when the size of the floating boundary is small, the distribution skews towards long periods, suggesting a minimum-period cutoff. As the floating-boundary size increases to 60% of the upper surface, however, a maximum-period cutoff appears.

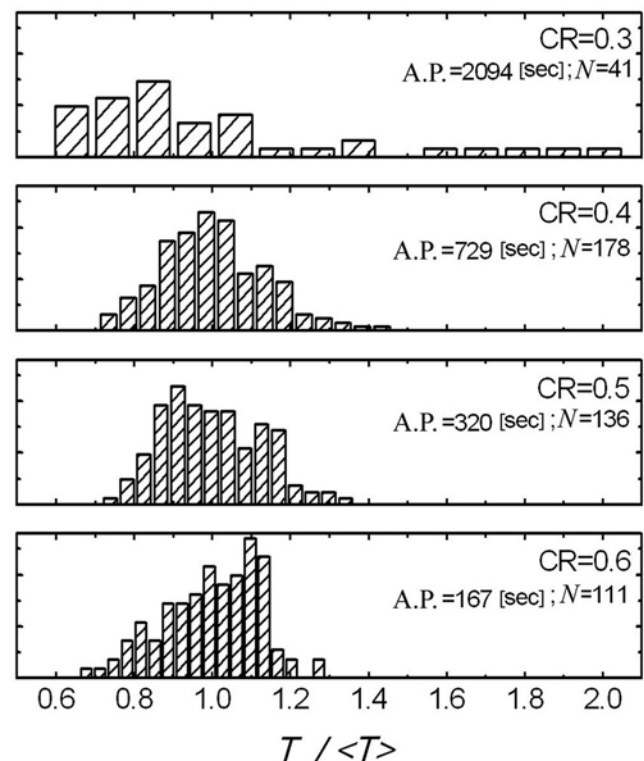


FIG. 12. Histogram of the oscillation periods for various floating boundary sizes for  $Ra=1.1 \times 10^9$ . The distribution is skewed towards long times for small boundary sizes and towards short times for larger sizes. A.P. is the average period over  $N$  oscillations.

#### 4. The effect of the floating boundary's thermal conductivity

The floating boundary size determines the length, regularity, and distribution of the oscillation period. Surprisingly, the thermal conductivity of the floating boundary itself does not affect the qualitative behavior of the coupled system.

In a test experiment, we use a thin aluminum floater (6.9 cm wide, 15 cm long, and 0.06 cm thick) instead of the plastic floater. We observe oscillations that resemble those for plastic floaters, even though the conductivity of the aluminum floater is about 1500 times greater than that of the plastic floater. The heat flux through the metal floater is increased, but by only 45% compared to that through the plastic floater. Since the heat transfer contrast between the free fluid surface and the covered surface with plastic floater is around 8:1, the contrast now with the aluminum floater is about 4:1. Thermal blanketing still persists and is significant. The underlying mechanism is that, as with the plastic floater, the aluminum floater produces a viscous boundary layer due to the no-slip boundary condition, effectively prohibiting convective mixing of the fluid and reducing the vertical heat exchange. So that, even for a perfect thermally conducting floater there should still be a viscous boundary layer that sticks to the floating boundary and thus still exhibits the thermal blanketing effect.

As a result, with an aluminum floating boundary, the oscillation period increases by about 30%, consistent with a numerical geophysical study<sup>15</sup> that showed that the insulating effect is insensitive to the conductivity of the overlying continent.

#### IV. DISCUSSION AND CONCLUSION

Large-scale flow patterns in a turbulent, thermally convecting fluid are almost stationary, rarely changing in the absence of a freely moving boundary. A free boundary causes regular oscillations, even for highly turbulent thermal flows at  $Ra \sim 10^{7-9}$ . These oscillations reflect large-amplitude feedback between the large-scale circulation, the thermal blanketing of the free boundary and the viscous drag upon it. Signatures of thermal fluctuation in the oscillation include imperfect periodicity, fluctuating temperatures and velocities and complex flow patterns at small scales.

The geological problem of continental drift and the Wilson cycle<sup>22</sup> initially motivated this experiment. While the direct quantitative relevance of our tabletop experiment to continental drift is far from clear, our experiments capture the essence of the physical mechanisms at play. We now briefly compare our experiment and mantle convection inside the Earth, drawing an analogy between the nearly periodic oscillation and the Wilson cycle.

Wilson found evidence that the Atlantic has closed and reopened nearly periodically with a period of about 300-500 million years. In our experiment, the Rayleigh number is in the same range as it is for the Earth,<sup>8,9</sup>  $Ra \sim 10^9$ . As mentioned above (Sec. III C), the heat transfer ratio between the insulating boundary and the free fluid surface is quite similar to that of the Earth. The Prandtl number,  $Pr = \nu/\kappa$ , differs greatly, since it is about  $10^{23}$  for the Earth<sup>8</sup> and only about 3

in our experiment. Though earlier works<sup>33,37,38</sup> found the Prandtl number not to be crucial to heat flux, it affects the convection speed (or Reynolds number). How to simulate extremely high Prandtl number convection (mantle convection) with low Prandtl number fluids (fluids typically used in laboratories) is still an open question.

The rheology of the Earth's mantle certainly differs from the fluid we study: each piece of oceanic lithosphere moves largely as a whole, while the working fluid in our experiment mixes freely with the bulk at any location. Also, the convective mantle is non-Newtonian. Additionally, the heating source and its distribution inside the Earth differ from what we realize in this experiment, where the heat flux comes from a heated bottom plate. For the Earth, 80% of heating is generated by radioactive decay of unstable elements inside the convective mantle and 20% from the potential energy (heat) trapped when the Earth first formed.<sup>8</sup>

We now compare the time scales of our experiment and the Earth. In our experiment the oscillation period directly relates to the size of the convection cell and its flow speed. At  $Ra = 1.1 \times 10^9$ , average flow speed  $\langle V \rangle = 1.8$  cm/s, and fluid depth  $D = 11.3$  cm, the time for one circulation around an aspect-ratio one eddy is approximately  $4D/\langle V \rangle = 25$  s. For floating boundary size  $l = 1.6D$  (or  $l = 0.5L$ ), the total number of circulations during one oscillation period is  $300 \text{ s}/25 \text{ s} \sim 12$ , so the convection needs about six rounds of circulation to organize a bulk flow pattern once the floater has moved to a new position. For the Earth, we know that the mantle convection speed<sup>8</sup> is of the order  $\langle V_E \rangle = 5$  cm/year. Assuming that convection involves the entire depth of the mantle,  $D_M = 3000$  km, one circulation takes about  $Tr = 4D_M/\langle V_E \rangle \sim 240$  m.y. Given that the average length of the Wilson cycle is 400 m.y., the number of circulations is less than two for each period, seemingly too short for the mantle to respond to the changed continent positions: less than one circulation is required to modify the large-scale pattern of mantle convection. If we consider a layered convection model<sup>39,40</sup> however, a convective mantle of 660 km depth would allow about eight circulations during one oscillation period, which seems somewhat more reasonable. Our experimental results thus favor shallow mantle convection in a layered configuration. However, we should bear in mind that the complexity of the Earth is much greater than that of our model system, so that any such conclusion is provisional and tentative.

It should be noted that, in the current experimental work, we limit ourselves to a fixed aspect ratio:  $L/D = 3.2$ . For simplicity, the choice of this aspect ratio was made to accommodate fewer than four large-scale eddies. Moreover, our choice of aspect ratio is similar to that of some earlier numerical models by Lowman and Jarvis.<sup>10,11,15</sup> In one of our ongoing experiments, we extend the aspect ratio to  $10 > L/D > 5.6$ . We still observe semiregular oscillations. Since this experiment is conducted in an annular geometry, we decided to leave its results out of the current report. Similarly, in another ongoing experiment at  $L/D = 1$ , we also observe robust oscillations. The experimental conditions are different from what are used in the current report: there, the free-



FIG. 13. Measurement positions. Dashed lines indicate positions of line scans, when the floating boundary stays put at the upper-left corner. The two squares show the positions of pointwise measurements when the boundary is free to move.

moving boundary (a collection of hard spheres) is at the bottom of the convection cell.

Although we have identified the physical mechanisms responsible for the phenomena observed in our experiment, we realize that a mathematical model is useful to better understand the physics involved. In fact, we have recently developed a low-dimensional model that qualitatively captures the essence of the dynamics described in this work. It is a phenomenological model that takes into account the floater position, floater velocity, the upwelling flow position (the dividing line between the two competing eddies), flow speed, the boundary layer thickness, etc. It is a set of linear equations with parameters (coefficients) taken directly from the current experiment. We have decided to submit a paper on the modeling aspect of this work elsewhere as a separate work. This model predicts the behavior of the coupled system, with features such as regular oscillations and also a transition to a nonoscillatory state, which was recently discovered.

In conclusion, a movable boundary in thermal convection spontaneously stimulates a convective fluid to oscillate. The oscillation emerging from thermal turbulence is robust, and its physical origin well understood. In future work, we intend to study multiple free boundaries interacting with each other, mediated by thermal convection. Also, we will look at the dynamics of floating boundaries with no lateral bounds in an annular convection cell.

### ACKNOWLEDGEMENTS

We wish to thank A. Libchaber, T. Bringley, B. Liu, J. Psaute, N. Ribe, D. Rothman, and M. Shelley for fruitful discussions. We wish to thank also both anonymous referees for their many helpful suggestions on our first manuscript. The project was partially supported by the Department of Energy (DE-FG0200ER25053), and partly by startup funds from New York University.

### APPENDIX

Figure 13 locates the measurement positions in all of our experiments.

#### 1. The design of the service tank

The service tank compensates for the exact amount of water the convection cell loses to evaporation (Fig. 14).

We first degas clean water by either boiling or ultrasonic heating, and place it in the service tank. This tank is divided into two chambers with a leakproof partition. A small water pump, working at 60 ml/min, constantly pumps water from the bigger chamber (the reservoir, left) to the smaller one (right). Between the right chamber and the convection cell, a siphon (a 4 mm diam tube) levels the fluid heights precisely. Due to the extremely small rate of evaporation in the convection cell, the water constantly overflows the top of the

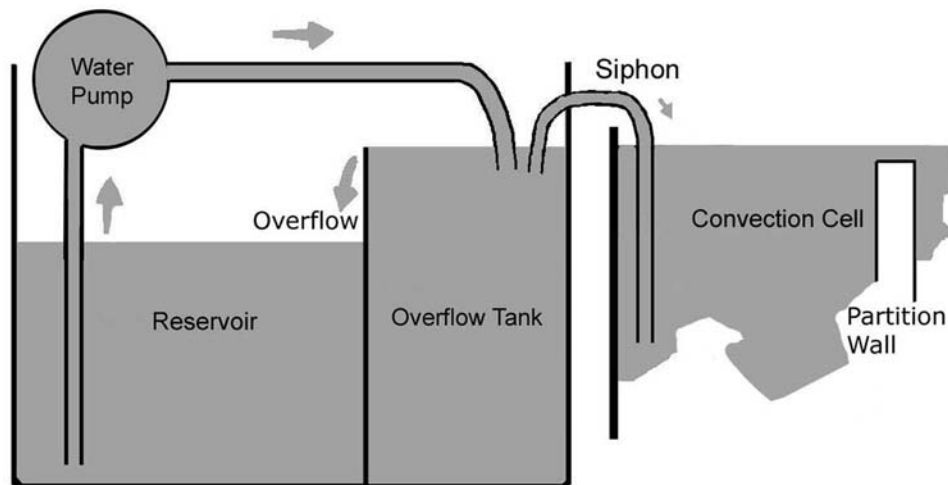


FIG. 14. The design of the service tank. The service tank is divided into two chambers. A small water pump brings water from the left chamber to the right. The right chamber connects to the convection cell through a siphon made of thin plastic tube. Since the flow rate to the convection cell is very low, water in the right chamber overflows to the left, maintaining a precise fluid level until the fluid on the left is consumed (not to scale).

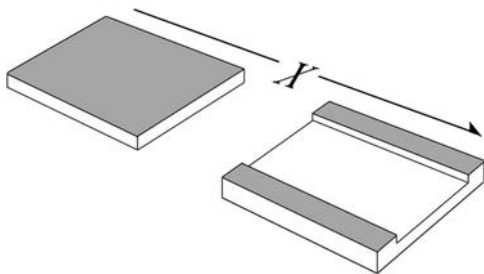


FIG. 15. Two types of floating boundaries. Only the shaded top surface is exposed to the air, while the rest is submerged in the bulk fluid. All edges are sharp so that they “pin” fluid contact lines, keeping the floater afloat even though it is denser than the fluid.

partition wall inside the service tank, maintaining the height of the water level in the right chamber and the convection cell, at all times. The height of the partition in the service tank determines the water level in the convection cell.

This design is maintenance free, not requiring fine-tuning of the pump rate. Before water from the service tank diffuses into the central convection cell, it is preheated in the side chamber to the bulk temperature. The extremely low flow rate (1.0-2.5 ml/min) and our unique arrangement cause negligible thermal and mechanical disturbances. The 4 l reservoir is sufficiently large that even at the highest Rayleigh numbers,  $Ra \sim 10^9$ , we need to add water only at intervals of about 20 h.

## 2. The design of the floating boundaries

Our experiment can use two types of floaters. As shown in Fig. 15, a flat acrylic rectangle can float on water if all top edges are sharp enough. This design is simple but has some drawbacks. A small quantity of surfactant molecules can impede the free motion of the floater due to surface elasticity. As the floater moves to the right, it forces surfactant molecules to the right, increasing the surfactant concentration on the right side and decreasing the surface tension. The opposite happens on the left side. This effect then creates an imbalance of surface tension that reduces the motion of the floating boundary. This effect is significant when the water is contaminated.

To avoid or greatly reduce this effect and increase tolerance to surface pollution, we developed a new design for the free-moving floater. In Fig. 15, the floater on the right is shaped like an inverted, compressed “II.” The two thin strips exposed to air allow the floater to stay afloat. Between the strips, the wide channel allows water to pass through. Pollutants and surfactant molecules can now cross the floater. Using this floater, our experiment is highly tolerant of impurities on the fluid surface. When the water is clean, the two types of floaters produce identical results.

Each floater is 6.9 cm wide and 0.65 cm thick. The floater is centered along the short dimension of the convection cell by a slight repulsive force. Along the long side of the convection cell, the floater is free; it is not affected by any of the side walls until it hits a submerged partition.

## 3. Heat transport through the surfaces: Thermal blanketing

Inside a moving fluid, the heat flux in the vertical (along the  $z$  axis) direction is<sup>41</sup>

$$J_z = C_p \rho \langle V_z(t) \cdot [T(t) - \bar{T}] \rangle_t - \chi \frac{\partial \bar{T}}{\partial z}.$$

Here,  $\langle \rangle_t$  denotes an average over time.  $C_p$  and  $\rho$  are the fluid's heat capacity and density,  $\bar{T}$  is the time-averaged temperature,  $V_z(t)$  is the vertical component of velocity,  $\chi$  is the thermal conductivity of water, and  $\partial \bar{T} / \partial z$  is the temperature gradient in the vertical direction. Within the thermal boundary layer, where  $V_z(t)$  diminishes, the above equation reduces to  $J_z = -\chi (\partial \bar{T} / \partial z)$ . We estimate the heat flux in our experiment using temperature profiles measured within the thermal boundary layers.

To check this result under the fixed floating boundary, we used two thermistors separated by 1.5 mm as two arms in a Wheatstone bridge and a lock-in amplifier. The thermistors do not shadow each other in the vertical direction. The detection measures the instantaneous temperature difference and local temperature gradient from which we can calculate the heat flux.

The latent heat needed to evaporate the water supplied from the service tank gives a lower limit estimate of the heat loss at the fluid surface. The difference between the input heat flux through the bottom plate and the heat flux through the fixed floating boundary, assuming no thermal leakage on the four vertical sides, gives an upper limit.

<sup>1</sup>See, for example, E. L. Koschmieder, *Bénard Cell and Taylor Vortices* (Cambridge University Press, New York, 1993).

<sup>2</sup>Lord Rayleigh, “On convection currents in a horizontal layer of fluid when the higher temperature is on the under side,” *Philos. Mag.* **32**, 529 (1916).

<sup>3</sup>W. V. R. Malkus, “Discrete transitions in turbulent convection,” *Proc. R. Soc. London, Ser. A* **225**, 185 (1954).

<sup>4</sup>R. Krishnamurti and L. N. Howard, “Large-scale flow generation in turbulent convection,” *Proc. Natl. Acad. Sci. U.S.A.* **78**, 4 (1981).

<sup>5</sup>M. Sano, X.-Z. Wu, and A. Libchaber, “Turbulence in helium-gas free-convection,” *Phys. Rev. A* **40**, 6421 (1989).

<sup>6</sup>D. J. Stevenson, “Mars’ core and magnetism,” *Nature* **412**, 214 (2001).

<sup>7</sup>M. T. Zuber, “The crust and mantle of Mars,” *Nature* **412**, 220 (2001).

<sup>8</sup>D. L. Turcotte and G. Schubert, *Geodynamics* (Cambridge University Press, New York, 2002).

<sup>9</sup>M. Gurnis, “Large-scale mantle convection and the aggregation and dispersal of supercontinents,” *Nature* **332**, 695 (1988).

<sup>10</sup>J. P. Lowman and G. T. Jarvis, “Mantle convection flow reversals due to continental collisions,” *Geophys. Res. Lett.* **20**, 2087 (1993).

<sup>11</sup>S. D. King, J. P. Lowman, and C. W. Gable, “Episodic tectonic plate reorganizations driven by mantle convection,” *Earth Planet. Sci. Lett.* **203**, 83 (2002).

<sup>12</sup>J. X. Mitrovica, “Plate-tectonics underpins supercontinent break-up,” *Phys. World* **7**, 35 (1994).

<sup>13</sup>F. H. Busse, “A model of time-periodic mantle flow,” *Geophys. J. R. Astron. Soc.* **52**, 1 (1978).

<sup>14</sup>C. Grigné and S. Labrosse, “Effects of continents on earth cooling: Thermal blanketing and depletion in radioactive elements,” *Geophys. Res. Lett.* **28**, 2707 (2001).

<sup>15</sup>J. P. Lowman and G. T. Jarvis, “Mantle convection models of continental collision and breakup incorporating finite thickness plates,” *Phys. Earth Planet. Inter.* **88**, 53 (1995).

<sup>16</sup>P. Davy, A. Sornette, and D. Sornette, “Some consequences of a proposed fractal nature of continental faulting,” *Nature* **348**, 56 (1990).

<sup>17</sup>R. W. Griffiths, R. I. Hackney, and R. D. Vanderhilst, “A laboratory in-

- vestigation of effects of trench migration on the descent of subducted slabs," *Earth Planet. Sci. Lett.* **133**, 1 (1995).
- <sup>18</sup>D. W. Oldenburg and J. N. Brune, "Ridge transform fault spreading pattern in freezing wax," *Science* **178**, 301 (1972).
- <sup>19</sup>R. Ragnarsson, J. L. Ford, C. D. Santangelo, and E. Bodenschatz, "Rifts in spreading wax layers," *Phys. Rev. Lett.* **76**, 3456 (1996).
- <sup>20</sup>J. A. Whitehead, "Moving heaters as a model of continental drift," *Phys. Earth Planet. Inter.* **5**, 199 (1972).
- <sup>21</sup>J. Zhang and A. Libchaber, "Periodic boundary motion in thermal turbulence," *Phys. Rev. Lett.* **84**, 4361 (2000).
- <sup>22</sup>J. T. Wilson, "Did the Atlantic close and then re-open?" *Nature* **211**, 676 (1966).
- <sup>23</sup>B. A. Grzybowski, N. Bowden, F. Arias, H. Yang, and G. M. Whitesides, "Modeling of menisci and capillary forces from the millimeter to the micrometer size range," *J. Phys. Chem. B* **105**, 404 (2001).
- <sup>24</sup>W. J. Yang, *Handbook of Flow Visualization* (Taylor & Francis, New York, 2001), and references therein.
- <sup>25</sup>G. Zocchi, E. Moses, and A. Libchaber, "Coherent structures in turbulent convection, an experimental study," *Physica A* **166**, 387 (1990).
- <sup>26</sup>X.-L. Qiu and P. Tong, "Large-scale velocity structures in turbulent thermal convection," *Phys. Rev. E* **64**, 036304 (2001).
- <sup>27</sup>D. A. Nield, "Surface tension and buoyancy effects in cellular convection," *J. Fluid Mech.* **19**, 341 (1964).
- <sup>28</sup>M. C. Cross and P. C. Hohenberg, "Pattern formation outside of equilibrium," *Rev. Mod. Phys.* **65**, 851 (1993), and references therein.
- <sup>29</sup>D. L. Anderson, "Hotspots, polar wander, Mesozoic convection and the geoid," *Nature* **297**, 391 (1982).
- <sup>30</sup>C. Pinet, C. Jaupart, J. C. Mareschal, C. Gariépy, G. Bienfait, and R. Lapointe, "Heat flow and structure of the lithosphere in the eastern Canadian shield," *J. Geophys. Res.* **96**, 19941 (1991).
- <sup>31</sup>X.-L. Qiu, X.-D. Shang, P. Tong, and K.-Q. Xia, "Velocity oscillations in turbulent Rayleigh-Bénard convection," *Phys. Fluids* **16**, 412 (2004).
- <sup>32</sup>S. Cioni, S. Ciliberto and J. Sommeria, "Strongly turbulent Rayleigh-Bénard convection in mercury: comparison with results at moderate Prandtl number," *J. Fluid Mech.* **335**, 111 (1997).
- <sup>33</sup>S. Grossmann and D. Lohse, "Scaling in thermal convection: A unifying theory," *J. Fluid Mech.* **407**, 27 (2000); "Thermal convection for large Prandtl number," *Phys. Rev. Lett.* **86**, 3316 (2001).
- <sup>34</sup>S. Lam, X.-D. Shang, S.-Q. Zhou, and K.-Q. Xia, "Prandtl number dependence of the viscous boundary layer and the Reynolds numbers in Rayleigh-Bénard convection," *Phys. Rev. E* **65**, 066306 (2002). (Note: The Reynolds number for the large-scale flow is found as  $Re = 1.1 Ra^{0.43} Pr^{-0.76}$ . The experiment is carried out at Prandtl numbers between 6 and 102.7.)
- <sup>35</sup>S. Ashkenazi and V. Steinberg, "High Rayleigh number turbulent convection in a gas near the gas-liquid critical point," *Phys. Rev. Lett.* **83**, 3641 (1999). (Note: This experiment covers  $1 < Pr < 93$  and  $10^9 < Ra < 10^{14}$ . They found a scaling:  $Re = 2.6 Ra^{0.43} Pr^{-0.75}$ .)
- <sup>36</sup>W. Feller, *An Introduction to Probability Theory and Its Applications*, Vol. 1 (Wiley, New York, 1968).
- <sup>37</sup>G. Ahlers and X. Xu, "Prandtl-number dependence of heat transport in turbulent Rayleigh-Bénard convection," *Phys. Rev. Lett.* **86**, 3320 (2001).
- <sup>38</sup>K.-Q. Xia, S. Lam, and S.-Q. Zhou, "Heat-flux measurement in high-Prandtl-number turbulent Rayleigh-Bénard convection," *Phys. Rev. Lett.* **88**, 064501 (2002).
- <sup>39</sup>R. Peltier and L. P. Solheim, "Mantle phase-transitions and layered chaotic convection," *Phys. Rev. Lett.* **19**, 321 (1992).
- <sup>40</sup>L. Wen and D. L. Anderson, "Layered mantle convection: A model for geoid and topography," *Earth Planet. Sci. Lett.* **146**, 367 (1997).
- <sup>41</sup>H. Tennekes and J. L. Lumley, *A First Course in Turbulence* (MIT Press, Cambridge, MA, 1972).